To be published in Journal of the Optical Society of America B:

Time-domain numerical modeling of THz receivers based on photoconductive antennas

E. MORENO[1,*], Z. HEMMAT[2,*], J.B. ROLDÁN[3,*], M. F. PANTOJA[1,*], A. R. BRETONES[1,*], AND S. G. GARCÍA[1,*]

[1] Department of Electromagnetism and Matter Physics, University of Granada, Granada 18071, Spain
[2] Department of Electrical Engineering, Sharif University of Technology, Tehran, Iran
[3] Department of Electronic and Computers Technology, University of Granada, Granada 18071, Spain
[*] Corresponding author: E. Moreno (enrique@moreno.ws), Z. Hemmat (zahra_hemmat@ee.sharif.edu), J.B. Roldán (jroldan@ugr.es), M. F. Pantoja (mario@ugr.es), A. R. Bretones (arubio@ugr.es) and S. G. García (salva@ugr.es)

We present here a simulator that solves the main semiconductor charge and transport equations coupled to Maxwell equations to study receivers based on photoconductive antennas (R-PCAs). Making use of this tool we were able to correctly characterize the operation of these antennas. In doing so, we compared simulations with the results of the semi-empirical expression $I_{THz}(t) \propto \sigma_c(t) * E_{THz}(t)$ employed to evaluate the detected photo-current by means of the convolution between the photoconductivity in the receiver and the electric field linked to the emitter antenna. We were able to accurately reproduce experimental data with our simulation tool. These kind of tools are essential to model photoconductive antennas, a fundamental step needed for the development of terahertz time domain spectroscopy (THz-TDS) applications based on PCAs.

OCIS codes: 040.2235 Terahertz (THz),040.5160 photoconductive antenna (PCA), 040.0040 receivers, 300.6500, 300.6495 terahertz time domain spectroscopy (THz-TDS), 110.6795 terahertz imaging (THz-I), 000.4430 hybrid FDTD methods.

1. INTRODUCTION

Terahertz time domain spectroscopy (THz-TDS) and imaging (THz-I) have been subject of intense research in the last few years. The application of these technologies have led to many promising applications with a strong future potential [1–5]. THz-TDS and THz-I techniques have been employed in applications that extract information from materials that can not be obtained by using other techniques, this was achieved by analyzing their interaction with terahertz electromagnetic fields [6–9]. Although there exist a broad variety of commercial systems and applications for THz-TDS and THz-I, there are many challenges to be solved in the current state-of-the-art terahertz technology. In this respect, some of the issues that have to be addressed are the following: production of compact systems operating with terahertz high power sources with lower prices, more efficient emitters and receivers with lower noise levels, exploration of techniques to mitigate scattering in THz-TDS, etc. [10–12]. In addition, the analysis of the reception process in photoconductive antennas (PCAs) is also a key subject that has to be studied in depth. In this context, we can check how scattering mitigation techniques are really working over the true absorption spectra measured in a receiver based on a PCA. In this paper we deal with this

problem, i.e., the analysis and characterization of reception processes in PCAs. To do so we have developed a new numerical method based on FDTD [13]. The PCA emission has been already studied [14–20]. There are numerical and experimental studies of receivers based on PCAs [19, 21–24], however, as far as we know, the lack of simultaneously simple and accurate numerical methods to simulate reception processes is one of the issue of major concerns in THz-TDS and THz-I studies. That is what we do here; for the development of the numerical method presented we have dealt with the usual trade-off, simplicity vs. accuracy, in order to address a realistic description of a receiver within a feasible and reasonable numerical approach.

In the last few years, several attempts to improve THz-TDS and THz-I technology have been published [25–28] by means of high cost experimental research studies, both in time and resources. It is well-known that a numerical tool can help to improve many facets of this technology at a low cost. Additionally, a numerical tool can supply extra information useful to understand the inner mechanisms of the physical processes undergoing the PCA operation, this knowledge is essential to take into account in the broad terrain of antennas design [29].

In general, the use of photoconductive devices have been assumed to be contextualized in the high power and high fre-

quency application realms. In the high-power domain, wide band-gap materials such as GaN and SiC are used for optically-triggered power semiconductor devices [30, 31]. For high-frequency applications, narrow band-gap materials like LT-GaAs are used in photoconductive layers in THz photoconductive antennas [32–34].

In this paper we will simulate receiving PCAs made of LT-GaAs
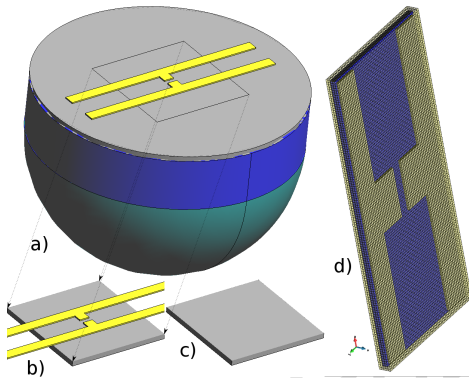
Fig. 1. (a) Photoconductive antenna formed by a photo-layer of LT-GaAs on SI-GaAs substrate and a dielectric lens under the substrate. (b) PEC contact on the photo-zone. (c) The photo-zone. (d) Computational domain simulated.

which are illuminated with plane waves generated in another PCAs, the latter antennas were numerically described in a previous work [20]. In [20] the photocurrents in non-biased PCAs were obtained by convolving the electric field radiated by the emitter antenna with the photoconductivity in a non-biased PCA. Here we follow this approach by comparing the simulated profile of the current in the receiver with the convolution of the electric field radiated by the emitter antenna and the photoconductivity in the receiver and, obviously, both profiles with experimental data [35, 36].

In the calculations presented here, the PCA lens and the semi-insulator substrate are not taken into consideration. We do so after demonstrating that both PCA components can be neglected in detection processes with normal incidence of the radiated field. This latter result is important for the development of a simulation tool to study, in direct sampling detection [22, 24], the Signal to Noise Ratio (SNR) with a particularly simple computational domain (see Fig. 1(d)) in a realistic manner. As is well known SNR is related with the carriers lifetime and mobility, the laser shot noise, Johnson-Nyquist noise... [21, 22, 37–39]; therefore, the simulation tool presented allows to study all these components in relation to SNR. These features can be of great help in connection to the design analysis of receivers based on PCAs.

The organization of the paper is as follows: in Section 2, we introduce the numerical approach employed by defining the photo-zone region, showing how to calculate the electric field radiated by the simulated dipoles, and explaining the method to simulate reception processes with PCAs; in section 3 we describe the main features of our simulator and show how to calculate the photocurrent. In section 4 the main results are presented and discussed and finally, in section 5 the conclusions are drawn.

## 2. TRANSIENT PROCESS CHARACTERIZATION

In Figure 1(a) we show a complete PCA, consisting of a photoactive layer (LT-GaAs) grown on a semi-insulating substrate

(SI-GaAs) placed on a dielectric lens (Polyethylene). On the photoactive layer, metal contacts are deposited to bias the emitter PCA and measure the intensity of current (in a receiver based on a PCA). Emitters and receivers are illuminated by a laser just at the gap between the metal contacts. Therefore, the main change in photoconductivity, and hence in the current density, takes place close to this gap. It is a zone (we analyze in 3D) that involves a specific region of the photoactive layer, located under the gap between the metal contacts.

This is the area christened photo-zone and illustrated in Figure 1(c). In this work, as in previous ones [20, 29, 40], the entire computational domain consists of the photo-zone plus the metal contacts. The sketch in 1(d) shows one of the two computational simulated domains. As reported previously [41], ohmic contacts are employed for a better electron injection accounting for the reduction of the Schottky barrier height.

In summary, we do not simulate the entire PCA; instead, we simulate a part of the antenna, the photo-zone.

### A. Emitter PCA, the radiated field

(a)

(b)
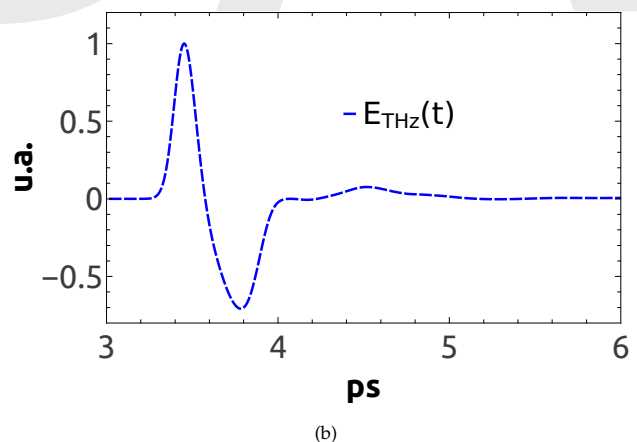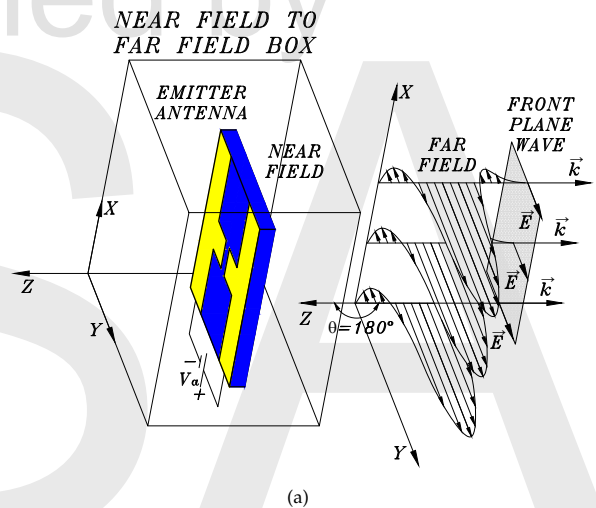
Fig. 2. (a) Near field to far field transform box surrounding the emitter antenna simulated in [20] (not to scale). (b) $E_{THz}(t)$ achieved in the previous work [20].

The numerical method of an emitter antenna to determine the field radiated by the dipole antenna has been described in Ref. [20]. To determine the radiated field we have used the

equivalence theorem and the algorithm of transformation from near-field to far-field (NF-FF) [13, 42]. Figure 2 shows a plane wave propagating into the Z-axis in the descending direction, linearly polarized in the Y-axis. The NF-FF transform has been performed in spherical coordinates towards the direction ($\theta = \pi$, $\varphi = 0$), where φ is measured from the X-axis. Under these circumstances $E_\theta \ll E_\varphi$ and we select $E_{THz}(t) \equiv E_y(t) \equiv E_\varphi(t)$ as the electric field sketched out in Figure 2(b).

B. R-PCA simulation
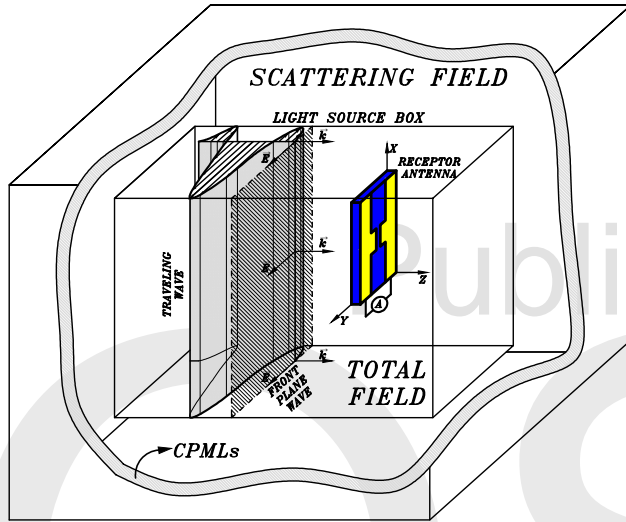
Fig. 3. Description of a plane wave, with the profile shown in Figure 2(b), that arrives to the receiving antenna photozone. The plane wave was generated by the light source, as described in [13]. This sketch is not shown to scale.

To simulate the reception process in the computational domain, the receiving antenna is placed inside the illumination box or light source box. Then we divide the computational domain into two regions. The region inside the illumination box is called region of total field whereas the outer region is called region of scattering field. These concepts are widely treated in the literature [13]. Figure 3 shows how the region of scattering field, the region outside the illumination box, is enclosed by CPMLs. We surround the illumination box in order to absorb the incident field reflected on the R-PCA and also to absorb its own radiated field by the R-PCA. In the region of total field, the use of the equivalence theorem allows considering that the radiation that reaches the receiver is a plane wave pulse, and therefore the reception process can be simulated under this assumption.

It should be noted that the plane wave is built with the profile radiated (at the far field region) by an emitter antenna. We simulate here two R-PCAs, a face to face (FF) dipole and an offset dipole [36]. In the previous work [20] we simulated a FF dipole. Its radiated filed profile (see Fig. 2b) is detected in this paper with another FF dipole corresponding with dipole III in [35]. In addition, an offset dipole has been simulated with the algorithms described in [20] and in this manuscript, and we have reproduced its radiated electric field making use of the same offset dipole geometry.

The first shot of the laser pulse must be synchronized with the front of plane wave in order to induce a rise photoconductivity at the moment the front of plane wave reaches the receiver.

There must be free charge carriers when the incident electric field interacts with the receiver to be swept. These carriers are moved by the electric field and generate an electric intensity of current (the calculation will be explained below) and allow a way to sample the incident electric field.

In addition, we can sample the incident electric field $E_{THz}(t)$ by using the semi-empirical equation 1. The convolution of the photoconductivity over the incident electric field highlight the most characteristic effect produced in the receiver by the incident electric field $E_{THz}(t)$. This approach has been widely employed [35, 43–46], the calculation is performed as follows:

$$I_{THz}(t) \propto \sigma_c(t) * E_{THz}(t) = \int \sigma_c(t-\tau)E_{THz}(\tau)d\tau \qquad \textbf{(1)}$$
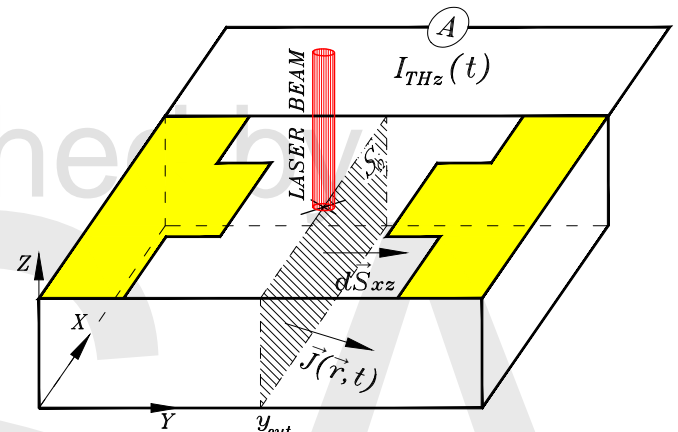
(a)
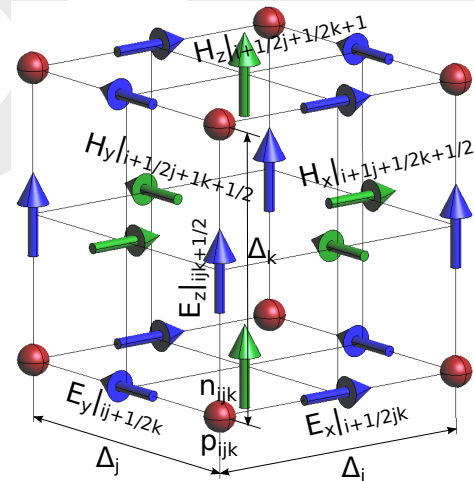
(b)

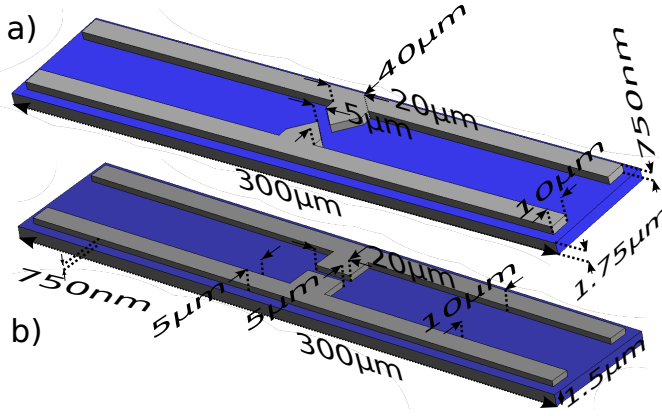**Fig. 4.** (a) Transverse cross section of the current density that crosses the metal contacts and allows the calculation of the intensity of current crossing the contacts. (b) Yee's cell.

We determined the photoconductivity in the photo-zone of a R-PCA with the following expression:

$$\sigma_c(t) = \iint_{S_\Omega} \sigma(x, y_{cut}, z, t) dS_{xz} \qquad \textbf{(2)}$$

where S_Ω is illustrated in Figure 4(a).

Fig. 5. a) Photo-zone of the offset dipole simulated in this paper. The emitter PCA whose radiated field has been detected with the offset dipole is another offset dipole. The main geometrical parameters of the offset dipole have been taken from [36]. In this case, both emitter and receptor have the same geometry. The thickness of the LT-GaAs substrate is $1.75\mu m$. b) Photo-zone of the face to face (FF) dipole also simulated in this work. This FF dipole corresponds with dipole III located in Table 1 of [35]. These sketches are not shown to scale. The thickness of the LT-GaAs substrate was assumed to be $1.5\mu m$.

Moreover, the above expression 2 was used in [20] to calculate the photoconductivity in the R-PCA.

3. NUMERICAL ALGORITHMS TO IMPLEMENT THE RECEPTION PROCESS ANALYSIS

The hybrid partial differential equation system that describes the transient regime in the photo-zone of a R-PCA is given by the following equations:

$$\mu \partial_t \vec{H}(\vec{r},t) = -\vec{\nabla} \wedge \vec{E}(\vec{r},t) \tag{3}$$

$$\varepsilon \partial_t \vec{E}(\vec{r},t) = \vec{\nabla} \wedge \vec{H}(\vec{r},t) - \vec{J}_T(\vec{r},t) \tag{4}$$

$$\partial_t n(\vec{r},t) = q^{-1}\vec{\nabla} \cdot \vec{J}_{nT}(\vec{r},t) + G(\vec{r},t) - R(\vec{r},t) \tag{5}$$

$$\partial_t p(\vec{r},t) = -q^{-1}\vec{\nabla} \cdot \vec{J}_{pT}(\vec{r},t) + G(\vec{r},t) - R(\vec{r},t) \tag{6}$$

The transient current can be obtained by means of the equation below,

$$\vec{J}_T(\vec{r},t) = \vec{J}_{nT} + \vec{J}_{nT} = \vec{J}_s(\vec{r},t) + (\sigma(\vec{r},t)+\sigma_0)\vec{E}(\vec{r},t) \tag{7}$$

where

$$\sigma(\vec{r},t) = q(\mu_{n0}n(\vec{r},t)+\mu_{p0}p(\vec{r},t))$$
$$\sigma_0 = q(\mu_{n0}n0+\mu_{p0}p0)$$
$$\vec{J}_s(\vec{r},t) = qV_T\left(\mu_{n0}\overrightarrow{\nabla n}(\vec{r},t)-\mu_{p0}\overrightarrow{\nabla p}(\vec{r},t)\right)$$

and $\sigma(\vec{r},t)$ stands for the conductivity transient term and σ_0 for the conductivity stationary term and $\vec{J}_s(\vec{r},t)$ for the source current. The source current here accounts for a current linked to diffusion process, unlike the previous work [20].

In receiving antennas, in contrast to the results shown in [20, 40], mobility models are not essential for the final result since the photo-zone is not biased by an external electric source. For our approach we have used the following values for $\mu_{n0} = 8000\frac{cm^{-2}}{Vs}$ and $\mu_{p0} = 400\frac{cm^{-2}}{Vs}$. We assumed that the N-type dopants in

the semiconductor are completely ionized at room temperature and hence, $n0 \simeq N_D = 10^{16}cm^{-3}$ and $p0 = \frac{n_i^2}{n0}$, where $n_i = 9 \cdot 10^6 cm^{-3}$. The generation, $G(\vec{r},t)$, and recombination rates, $R(\vec{r},t)$, are the same introduced in [20]. The laser temporal distribution σ_t in the generation rate is 80fs for the FF dipole and 115fs for the offset dipole.

A. Differential equations numerical solution: Discretization with FDTD

The temporal scheme for discretization in the time domain of partial differential equations 3-6 with FDTD was introduced in [20]. Time-space discretization of Maxwell-Ampere equation 4 along the X-axis and inside the photo-area by using the same type of Yee's cell [20] (the simulation approach followed was represented in Figure 4(b)) led us to the following equation:

$$E_x|_{i+\frac{1}{2},j,k}^{m+\frac{1}{2}} = Ca_x|_{i+\frac{1}{2},j,k}^m E_x|_{i+\frac{1}{2},j,k}^{m-\frac{1}{2}}$$

$$+Cb_x|_{i+\frac{1}{2},j,k}^m \left(\frac{H_z|_{i+\frac{1}{2},j+\frac{1}{2},k}^m - H_z|_{i+\frac{1}{2},j-\frac{1}{2},k}^m}{\delta_{y_j}} \right.$$

$$\left. -\frac{H_y|_{i+\frac{1}{2},j,k+\frac{1}{2}}^m - H_y|_{i+\frac{1}{2},j,k-\frac{1}{2}}^m}{\delta_{z_k}} - J_{sx}|_{i+\frac{1}{2},j,k}^m \right) \tag{8}$$

where the source current component along the X-axis direction is given by:

$$J_{sx}|_{i+\frac{1}{2},j,k}^m =$$
$$qV_T\left(\frac{\mu_{n0}\left(n_{i+1,j,k}^m - n_{i,j,k}^m\right) - \mu_{p0}\left(p_{i+1,j,k}^m - p_{i,j,k}^m\right)}{\Delta x_i} \right)$$

and the transient photoconductivity is described below: $\sigma_{i+\frac{1}{2},j,k}^m = q(\mu_{n0}n_{i+\frac{1}{2},j,k}^m +\mu_{p0}p_{i+\frac{1}{2},j,k}^m)$. In addition, coefficients $Ca_x|_{i+\frac{1}{2},j,k}^m$ and $Cb_x|_{i+\frac{1}{2},j,k}^m$ in equation 8 can be given as follows:

$$Ca_x|_{i+\frac{1}{2},j,k}^m =$$
$$\begin{cases} \frac{2\varepsilon-\Delta_t\left(\sigma_{i+\frac{1}{2},j,k}^m+\sigma_0\right)}{2\varepsilon+\Delta_t\left(\sigma_{i+\frac{1}{2},j,k}^m+\sigma_0\right)} & \text{if } 2\varepsilon \geq \Delta_t\left(\sigma_{i+\frac{1}{2},j,k}^m+\sigma_0\right) \\ \\ e^{-\frac{\Delta_t\left(\sigma_{i+\frac{1}{2},j,k}^m+\sigma_0\right)}{\varepsilon}} & \text{if } 2\varepsilon < \Delta_t\left(\sigma_{i+\frac{1}{2},j,k}^m+\sigma_0\right) \end{cases}$$

$$Cb_x|_{i+\frac{1}{2},j,k}^m =$$
$$\begin{cases} \frac{2\Delta_t}{2\varepsilon+\Delta_t\left(\sigma_{i+\frac{1}{2},j,k}^m+\sigma_0\right)} & \text{if } 2\varepsilon \geq \Delta_t\left(\sigma_{i+\frac{1}{2},j,k}^m+\sigma_0\right) \\ \\ \frac{1-e^{-\frac{\Delta_t\left(\sigma_{i+\frac{1}{2},j,k}^m+\sigma_0\right)}{\varepsilon}}}{\sigma_{i+\frac{1}{2},j,k}^m+\sigma_0} & \text{if } 2\varepsilon < \Delta_t\left(\sigma_{i+\frac{1}{2},j,k}^m+\sigma_0\right) \end{cases}$$

The discretization of the semiconductor continuity equations 5-6, in the time and the space domains is implemented by using the following equation:

$$n_{i,j,k}^{m+\frac{1}{2}} = n_{i,j,k}^{m-\frac{1}{2}} + q^{-1}\vec{\nabla} \cdot \vec{J}_{nT}|_{i,j,k}^m + G_{i,j,k}^m - R_{i,j,k}^m \tag{9}$$

$$p_{i,j,k}^{m+\frac{1}{2}} = p_{i,j,k}^{m-\frac{1}{2}} - q^{-1}\vec{\nabla} \cdot \vec{J}_{pT}|_{i,j,k}^m + G_{i,j,k}^m - R_{i,j,k}^m \tag{10}$$

where the explicit expression for the terms $\vec{\nabla} \cdot \vec{J}_n|_{i,j,k}^m$ and $\vec{\nabla} \cdot \vec{J}_{pT}|_{i,j,k}^m$ and the current divergence are detailed in the appendix A.

Finally, the boundary conditions are described in [20] with the equations 23 and 24. Taking into consideration all these contributions, we can calculate the flowing through the metal contacts on the surface S_Ω by means of the following equation (shown in Figure 4(a)):

$$I_{THz}(t) =$$
$$\int_0^{\nu_\gamma^{-1}} \iint_{S_\Omega} \sigma(x, y_{cut}, z, t-\tau) E_y(x, y_{cut}, z, \tau) dx dz d\tau \quad \textbf{(11)}$$

Where ν_γ is the laser's repetition rate equal to 82MHz in this work. By delaying the laser shooting time with respect to the incident electromagnetic field, we can shift the photoconductivity in time over the incident electromagnetic field. In this way we can sample the incident electromagnetic field as well as we do with the convolution (see the previous equation 1). Therefore, equation 11 is coherent with equation A1 in [22].
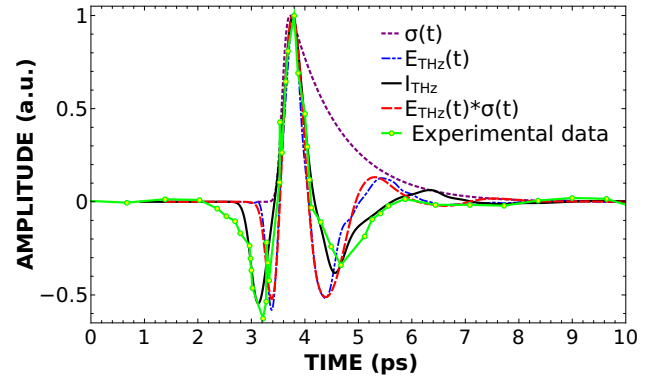
4. RESULTS AND DISCUSSION
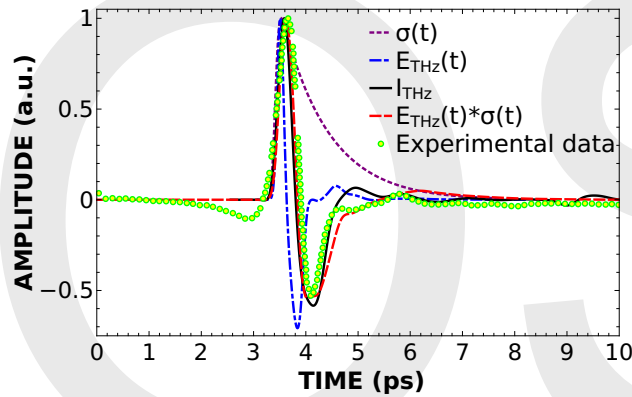
Fig. 6. Profile detected by the FF dipole. Experimental data are shown in green dots [35], the short dash violet line is used for the photoconductivity in the receiving antenna, the dash-dot blue profile shows the electric field (from Figure 2(b)), the dash red curve represents the convolution between the electric field (dash-dot blue) and the photoconductivity (dash violet) and the continuous black curve portrays the measured intensity of current for the receiver.

The receiver simulated with the FF dipole (see Fig. 5(b)) corresponds to dipole III described in [35]. Whereas the receiver simulated using the offset dipole (see Fig. 5(a)) is described in [36]. Figures 6 and 8 for the FF dipole, and Figures 7 and 9 for the offset dipole show the comparison between the simulated current $I_{THz}(t)$ (continuous black curve) in a receiving antenna and experimental data (green dots) for FF dipole [35] and offset dipole [36]. Moreover the convolution of incident electrical field hitting on the R-PCA and the photoconductivity of the receiver (red dash line) are also compared.

In this paper the detected current $I_{THz}(t)$ was obtained through a low level photon flux regime $5 \frac{W}{\mu m^2}$ and far from trap saturation conditions, so $I_{THz}(t)$ shows a direct-sampling-like behavior (the sampling falls between the direct-sampling and integrating-sampling but closer to direct-sampling) [24].

Fig. 7. Profile detected by the offset dipole. Experimental data are shown in green dots [36], the short dash violet line is used for the photoconductivity in the receiving antenna, the dash-dot blue profile shows the electric field (which has been simulated with the algorithms algorithms developed for emitters in [20]), the dash red curve represents the convolution between the electric field (dash-dot blue) and the photoconductivity (dash violet) and the continuous black curve portrays the measured intensity of current for the receiver.

The generation rate in the semiconductor is mainly governed by the photoelectric effect and does not depend much on the type of semiconductor substrate. Therefore, femto-second laser used for generation influences the temporal response of the conductivity in the receiver. Accordingly, the bandwidth that can be sampled depends on the duration of the laser pulses [22].
The main noise source related to the semiconductor substrate and its electrical properties is the Johnson-Nyquist noise. The Johnson-Nyquist noise current is inversely proportional to the square root of the average resistance of the device. Then, the main role played by the recombination rate in the receiver is related with the level of signal to noise ratio achieved [22].
In the emitter PCA, at points close to the gap, the density of photocurrent has got the same structure, in the time domain, that the photoconductivity. Therefore, by considering the Fourier transform interpretation, the generation process is linked to the higher frequencies radiated, and thus frequencies linked with the generation process have more energy than the emitter in the recombination stage. The generated electromagnetic field in an emitter PCA, in the travel along the LT-GaAs substrate suffers dispersion. The emitter PCA presents a conductivity which attenuates some frequencies generated, but more specifically, the higher ones. Apart from the emitter, the conductivity of the receiver photo-zone also increases its value along the reception process and attenuates frequency components. In the time domain, the conductivity of the emitter PCAs as well as the R-PCAs disperse the electromagnetic fields. Also the geometry or antenna structure, in a receiver, play an important role over the terahertz spectrum detected due to the resonance frequency [23]. We interpret that the difference between equation 1 and the equation 11 is largely due to the electric field. In the equation 1 the electric field does not suffer the same type of dispersion (time interpretation) neither the attenuation of its components (frequency interpretation) than in the equation 11, mainly because the electric field is modified by the receiver in a more realistic form. This fact is highlighted in Figures 8 and 9.
In this paper we do not take into account other dispersive media that are presented in these kind of devices: the semi-insulator

substrate and the lens. In spite of their low conductivities, they should not have been neglected. Their inclusion could explain why the experimental data profiles in Figures 8 and 9 have fewer frequency components than the simulated profiles, mainly in the most energetic region, for the higher frequencies. Also, the discrepancies between detected currents $I_{THz}(t)$ and experimental data could be explained by the role played by parameters that can not be described accurately in all the transport regimes considered here because of the lack of accurate models. In connection with this fact, the following comments should be considered. The lifetime of electrons was assumed to be $\tau_n = 0.3ps$ for the FF dipole and $\tau_n = 0.4ps$ for the offset dipole, in order to achieve the best result. In the case of the offset dipole, the reference [36] provides an approximate value for the laser temporal distribution $\sigma_t \sim 100fs$, but we have achieved better results using $\sigma_t = 115fs$. In addition, we assumed for our simulations the conventional semiconductor physical parameters, for all the different transport regimes considered.
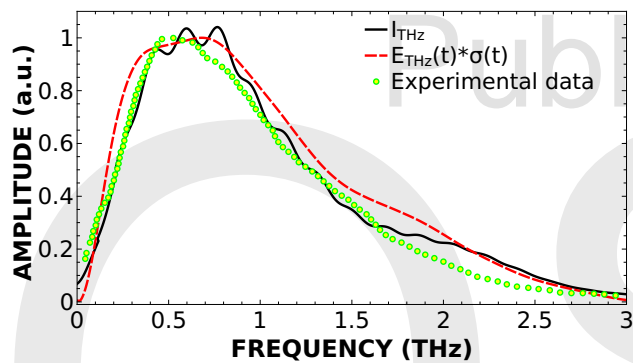
Fig. 8. Fourier transform of the profiles in Figure 6. Experimental data are shown in green dots [35], the dash red curve represents the convolution between the electric field (dash-dot blue) and the photoconductivity (dash violet) and the continuous black curve portrays the measured intensity of current for the receiver.
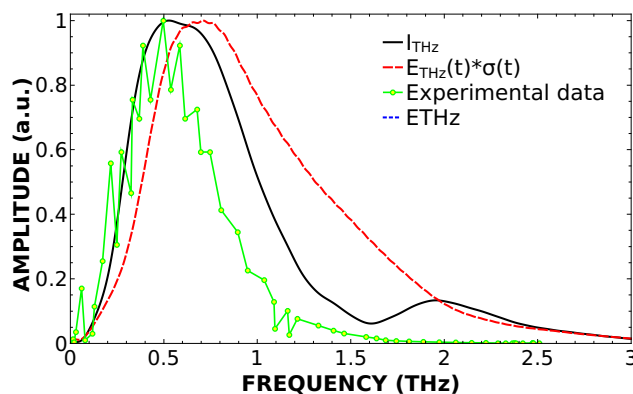
Fig. 9. Fourier transform of the profiles in Figure 7. Experimental data are shown in green dots [36], the dash red curve represents the convolution between the electric field (dash-dot blue) and the photoconductivity (dash violet) and the continuous black curve portrays the measured intensity of current for the receiver.

Moreover, it should be highlighted that dipole FF results fit experimental data much better than in the offset dipole case. Therefore, the drift-diffusion model reproduces the currents in better way in the case of the FF dipole. This might be linked to the role played by the mesh, since the mesh size employed to simulate both dipoles is similar. Hence, a less abrupt change in the electric field distribution (the case for the FF dipole) leads to more accurate results.

Notwithstanding, as can be seen, we can simulate the reception process accurately in a PCA with an FDTD approach. The calculation could be performed by modeling the charge transport in the semiconductor by means of the drift-diffusion model. In this way, FDTD algorithms provide enough accuracy in a faster manner than other complex methods based on Monte Carlo algorithms. Even though the drift-diffusion method approach might be considered out of its natural applicability frame, the versatility of the use of explicit compact mobility models and a realistic generation rate led us to model the physics in a successful and reasonable way.

The dispersive media, the SI-GaAs substrate and the lens, have not been take into account in our simulation. This fact could explain the narrower simulated $I_{THz}(t)$ profile obtained (solid black curve) in comparison with the experimental one (green dots).

In addition, these results show that the receiver photoconductivity could be considered a good approximation of the impulsive response of the own receiver [47]. Thus convolving any input, for instance the electric field reaching the receiver, with the receiver photoconductivity we get a magnitude proportional to the detected intensity of current $I_{THz}(t)$ in the receiver. This receiver with a linear behavior in relation to the terahertz input is explained by the linearity of the drift-diffusion model, equation 11 suggests this fact.

Our simulator allows simulation of a coherence reception process in R-PCAs, it means to know amplitude and phase simultaneously, without the need of kramers-kronig techniques [48]. Using a dispersive media model within the FDTD method with complex-conjugate pole-residue pairs [49], we can characterize, in the terahertz range, a dispersive media through its complex-conjugate pole-residue pairs comparing the simulated intensity of current I_{THz} with experimental data. This characterization can be useful in design and simulation of complex samples built with several media, mainly when these media are studied utilizing THz-TDS based on PCAs.

5. CONCLUSIONS

By means of three-dimensional device simulator [20] a new method to study reception processes in photoconductive antennas has been developed. The simulation approach is based on solving curl Maxwell equations and the semiconductor continuity equations for electrons and holes by means of an hybrid FDTD scheme.

A normalized result given by the semi-empirical expression $\sigma_c(t) * E_{THz}(t)$ has been compared with the simulated intensity of current $I_{THz}(t)$ and also with experimental data. Experimental data were accurately reproduced by simulations. The results that can be obtained with our simulation tool can help in the characterization of PCAs reception processes for future THz-TDS applications.

6. ACKNOWLEDGEMENTS

TIC-5327, P12-TIC-1442, and by the GENIL excellence network.

A. CURRENT DIVERGENCE CALCULATION

We calculated the current divergence with the help of Bernoulli's function $B(x) = \frac{x}{e^x - 1}$ as follows:

$$\vec{\nabla} \cdot \vec{J}_n|_{i,j,k}^m =$$

$$\frac{\mu_n|_{i+\frac{1}{2},j,k}}{\Delta x_i \delta_{x_i}} \left(B\left(\frac{-\Delta x_i}{V_T} Ex|_{i+\frac{1}{2},j,k}^m \right) n_{i+1,j,k}^m \right.$$

$$\left. - B\left(\frac{\Delta x_i}{V_T} Ex|_{i+\frac{1}{2},j,k}^m \right) n_{i,j,k}^m \right)$$

$$- \frac{\mu_n|_{i-\frac{1}{2},j,k}}{\Delta x_i \delta_{x_i}} \left(B\left(\frac{-\Delta x_{i-1}}{V_T} Ex|_{i-\frac{1}{2},j,k}^m \right) n_{i,j,k}^m \right.$$

$$\left. - B\left(\frac{\Delta x_{i-1}}{V_T} Ex|_{i-\frac{1}{2},j,k}^m \right) n_{i-1,j,k}^m \right)$$

$$+ \frac{\mu_n|_{i,j+\frac{1}{2},k}}{\Delta y_j \delta_{y_j}} \left(B\left(\frac{-\Delta y_j}{V_T} Ey|_{i,j+\frac{1}{2},k}^m \right) n_{i,j+1,k}^m \right.$$

$$\left. - B\left(\frac{\Delta y_j}{V_T} Ey|_{i,j+\frac{1}{2},k}^m \right) n_{i,j,k}^m \right)$$

$$- \frac{\mu_n|_{i,j-\frac{1}{2},k}}{\Delta y_j \delta_{y_j}} \left(B\left(\frac{-\Delta y_{j-1}}{V_T} Ey|_{i,j-\frac{1}{2},k}^m \right) n_{i,j,k}^m \right.$$

$$\left. - B\left(\frac{\Delta y_{j-1}}{V_T} Ey|_{i,j-\frac{1}{2},k}^m \right) n_{i,j-1,k}^m \right)$$

$$+ \frac{\mu_n|_{i,j,k+\frac{1}{2}}}{\Delta z_k \delta_{z_k}} \left(B\left(\frac{-\Delta z_k}{V_T} Ez|_{i,j,k+\frac{1}{2}}^m \right) n_{i,j,k+1}^m \right.$$

$$\left. - B\left(\frac{\Delta z_k}{V_T} Ez|_{i,j,k+\frac{1}{2}}^m \right) n_{i,j,k}^m \right)$$

$$- \frac{\mu_n|_{i,j,k-\frac{1}{2}}}{\Delta z_k \delta_{z_k}} \left(B\left(\frac{-\Delta z_{k-1}}{V_T} Ez|_{i,j,k-\frac{1}{2}}^m \right) n_{i,j,k}^m \right.$$

$$\left. - B\left(\frac{\Delta z_{k-1}}{V_T} Ez|_{i,j,k-\frac{1}{2}}^m \right) n_{i,j,k-1}^m \right) \quad \textbf{(12)}$$

and for holes,

$$\vec{\nabla} \cdot \vec{J}_p|_{i,j,k}^m =$$

$$\frac{\mu_p|_{i+\frac{1}{2},j,k}}{\Delta x_i \delta_{x_i}} \left(B\left(\frac{-\Delta x_i}{V_T} Ex|_{i+\frac{1}{2},j,k}^m \right) p_{i,j,k}^m \right.$$

$$\left. - B\left(\frac{\Delta x_i}{V_T} Ex|_{i+\frac{1}{2},j,k}^m \right) p_{i+1,j,k}^m \right)$$

$$- \frac{\mu_p|_{i-\frac{1}{2},j,k}}{\Delta x_i \delta_{x_i}} \left(B\left(\frac{-\Delta x_{i-1}}{V_T} Ex|_{i-\frac{1}{2},j,k}^m \right) p_{i-1,j,k}^m \right.$$

$$\left. - B\left(\frac{\Delta x_{i-1}}{V_T} Ex|_{i-\frac{1}{2},j,k}^m \right) p_{i,j,k}^m \right)$$

$$+ \frac{\mu_p|_{i,j+\frac{1}{2},k}}{\Delta y_j \delta_{y_j}} \left(B\left(\frac{-\Delta y_j}{V_T} Ey|_{i,j+\frac{1}{2},k}^m \right) p_{i,j,k}^m \right.$$

$$\left. - B\left(\frac{\Delta y_j}{V_T} Ey|_{i,j+\frac{1}{2},k}^m \right) p_{i,j+1,k}^m \right)$$

$$- \frac{\mu_p|_{i,j-\frac{1}{2},k}}{\Delta y_j \delta_{y_j}} \left(B\left(\frac{-\Delta y_{j-1}}{V_T} Ey|_{i,j-\frac{1}{2},k}^m \right) p_{i,j-1,k}^m \right.$$

$$\left. - B\left(\frac{\Delta y_{j-1}}{V_T} Ey|_{i,j-\frac{1}{2},k}^m \right) p_{i,j,k}^m \right)$$

$$+ \frac{\mu_p|_{i,j,k+\frac{1}{2}}}{\Delta z_k \delta_{z_k}} \left(B\left(\frac{-\Delta z_k}{V_T} Ez|_{i,j,k+\frac{1}{2}}^m \right) p_{i,j,k}^m \right.$$

$$\left. - B\left(\frac{\Delta z_k}{V_T} Ez|_{i,j,k+\frac{1}{2}}^m \right) p_{i,j,k+1}^m \right)$$

$$- \frac{\mu_p|_{i,j,k-\frac{1}{2}}}{\Delta z_k \delta_{z_k}} \left(B\left(\frac{-\Delta z_{k-1}}{V_T} Ez|_{i,j,k-\frac{1}{2}}^m \right) p_{i,j,k-1}^m \right.$$

$$\left. - B\left(\frac{\Delta z_{k-1}}{V_T} Ez|_{i,j,k-\frac{1}{2}}^m \right) p_{i,j,k}^m \right) \quad \textbf{(13)}$$

These expressions derive from [50] and were modified in [20] to be applied in the simulation of transient processes.

REFERENCES

1. H. Porte, D. Turchinovich, S. Persheyev, Y. Fan, M. Rose, and P. Jepsen, "On Ultrafast Photoconductivity Dynamics and Crystallinity of Black Silicon," Terahertz Science and Technology, IEEE Transactions on **3**, 331–341 (2013).

2. C. Seco-Martorell, V. López-Domínguez, G. Arauz-Garofalo, A. Redo-Sanchez, J. Palacios, and J. Tejada, "Goya’s artwork imaging with Terahertz waves," Opt. Express **21**, 17800–17805 (2013).

3. D. George, J. Knab, Y. He, M. Kumauchi, R. Birge, W. Hoff, and A. Markelz, "Photoactive Yellow Protein Terahertz Response: Hydration, Heating and Intermediate States," Terahertz Science and Technology, IEEE Transactions on **3**, 288–294 (2013).

4. T. Wang, P. Klarskov, and P. Jepsen, "Ultrabroadband THz Time-Domain Spectroscopy of a Free-Flowing Water Film," Terahertz Science and Technology, IEEE Transactions on **4**, 425–431 (2014).

5. C.-Y. Jen and C. Richter, "Doping Profile Recognition Applied to Silicon Photovoltaic Cells Using Terahertz Time-Domain Spectroscopy," Terahertz Science and Technology, IEEE Transactions on **4**, 560–567 (2014).

6. H.-B. Liu, Y. Chen, G. J. Bastiaans, and X.-C. Zhang, "Detection and identification of explosive RDX by THz diffuse reflection spectroscopy," Opt. Express **14**, 415–423 (2006).

7. K. Fukunaga, I. Hosako, M. Picollo, and Y. Kohdzuma, "Application of THz sensing to analysis of works of art for conservation," in "Microwave Photonics (MWP), 2010 IEEE Topical Meeting on," (2010), pp. 147–150.

8. M. Tsurkan, N. Balbekin, E. Sobakinskaya, A. Panin, and V. Vaks, "Terahertz spectroscopy of DNA," Optics and Spectroscopy **114**, 894–898 (2013).

9. R. Ullah, H. Li, and Y. Zhu, "Terahertz and {FTIR} spectroscopy of 'bisphenol a'," Journal of Molecular Structure **1059**, 255 – 259 (2014).

10. M. Kaushik, B. W.-H. Ng, B. M. Fischer, and D. Abbott, "Mitigating scattering effects in THz-TDS measurements," in "Infrared Millimeter and Terahertz Waves (IRMMW-THz), 2010 35th International Conference on," (2010), pp. 1–2.

11. C. Armstrong, "The truth about terahertz," Spectrum, IEEE **49**, 36–41 (2012).

12. M. Freebody, "Challenges Not Insurmountable for Terahertz Spectroscopy," Biophotonics **21**, 26–31 (2014).

13. A. Taflove and S. C. Hagness, *Computational Electrodynamics The Finite-Differences Time Domain Method* (2005).

14. E. Sano and T. Shibata, "Fullwave Analysis Of Picosecond Photoconductive Switches," Quantum Electronics, IEEE Journal of **26**, 372 – 377 (1990).

15. C. C. B. J. A. Reineix, M. Ariaudo, "Theoretical Analysis Of Photoconducting Dipole Antennas," Microwave and Optical Technology Letters **15**, 110–113 (1997).

16. Z.-S. P. M. T. K. Sakai, "Analysis Of THz Pulses Using The FDTD Calculation Method," Ultrafast Devices and Lasers **3940**, 184–191 (2000).

17. S. Hughes, M. Tani, and K. Sakai, "Vector Analysis Of Terahertz Transients Generated By Photoconductive Antennas In Near- And Far-Field Regimes," Journal of Applied Physics **93**, 4880–4884 (2003).

18. P. Kirawanich, S. Yakura, and N. Islam, "Study Of High-Power Wideband Terahertz-Pulse Generation Using Integrated High-Speed Photoconductive Semiconductor Switches," Plasma Science, IEEE Transactions on **37**, 219–228 (2009).

19. J. Zhang, W.-R. Ng, M. Tuo, M. Liang, D. Golish, M. Gehm, and H. Xin, "Theoretical and experimental study of a terahertz time-domain spectrometer based on photoconductive antenna," in "Radio Science Meeting (USNC-URSI NRSM), 2014 United States National Committee of URSI National," (2014), pp. 1–1.

20. E. Moreno, M. Pantoja, S. Garcia, A. Bretones, and R. Martin, "Time-Domain Numerical Modeling Of THz Photoconductive Antennas," Terahertz Science and Technology, IEEE Transactions on **PP**, 1–11 (2014).

21. E. Castro-Camus, J. Lloyd-Hughes, L. Fu, H. H. Tan, C. Jagadish, and M. B. Johnston, "An ion-implanted InP receiver for polarization resolved terahertz spectroscopy," Optics express **15**, 7047–7057 (2007).

22. E. Castro-Camus, L. Fu, J. Lloyd-Hughes, H. H. Tan, C. Jagadish, and M. B. Johnston, "Photoconductive response correction for detectors of terahertz radiation," Journal of Applied Physics **104**, 053113 (2008).

23. R. Yano, H. Gotoh, Y. Hirayama, S. Miyashita, Y. Kadoya, and T. Hattori, "Terahertz wave detection performance of photoconductive antennas: Role of antenna structure and gate pulse intensity," Journal of Applied Physics **97**, 103103 (2005).

24. E. Castro-Camus, M. B. Johnston, and J. Lloyd-Hughes, "Simulation of fluence-dependent photocurrent in terahertz photoconductive receivers," Semiconductor Science and Technology **27**, 115011 (2012).

25. G. Staats and U. Schade, "New structures for high resolution THz-imaging in medical applications," in "Nuclear Science Symposium Conference Record, 2008. NSS '08. IEEE," (2008), pp. 1741–1747.

26. J. Szelc and H. Rutt, "Near-Field THz Imaging and Spectroscopy Using a Multiple Subwavelength Aperture Modulator," Terahertz Science and Technology, IEEE Transactions on **3**, 165–171 (2013).

27. B.-Y. Ung, J. Li, H. Lin, B. Fischer, W. Withayachumnankul, and D. Abbott, "Dual-Mode Terahertz Time-Domain Spectroscopy System," Terahertz Science and Technology, IEEE Transactions on **3**, 216–220 (2013).

28. V. Sanphuang, W.-G. Yeo, J. Volakis, and N. Nahar, "THz Transparent Metamaterials for Enhanced Spectroscopic and Imaging Measurements," Terahertz Science and Technology, IEEE Transactions on **PP**, 1–7 (2014).

29. E. Moreno, M. Fernandez, A. Rubio Bretones, M. Cabello, and S. Gonzalez Garcia, "A Comparison Of The Performance Of THz Photoconductive Antennas," Antennas and Wireless Propagation Letters, IEEE **PP**, 1–1 (2014).

30. A. Meyer, A. Mojab, and S. Mazumder, "Evaluation of first 10-kv optical ETO thyristor operating without any low-voltage control bias," in "Power Electronics for Distributed Generation Systems (PEDG), 2013 4th IEEE International Symposium on," (2013), pp. 1–5.

31. A. Mojab, S. Mazumder, L. Cheng, A. Agarwal, and C. Scozzie, "15-kV single-bias all-optical ETO thyristor," in "Power Semiconductor Devices IC's (ISPSD), 2014 IEEE 26th International Symposium on," (2014), pp. 313–316.

32. M. Tani, K.-S. Lee, and X.-C. Zhang, "Photoconductive detection of THz radiation using two-step photoabsorption in LT-GaAs," in "Lasers and Electro-Optics, 2000. (CLEO 2000). Conference on," (2000), pp. 529–530.

33. J. Zhang, Y. Hong, S. Braunstein, and K. Shore, "Terahertz pulse generation and detection with LT-GaAs photoconductive antenna," Optoelectronics, IEE Proceedings - **151**, 98–101 (2004).

34. L. Hou and W. Shi, "An LT-GaAs Terahertz Photoconductive Antenna With High Emission Power, Low Noise, and Good Stability," Electron Devices, IEEE Transactions on **60**, 1619–1624 (2013).

35. K. S. Masahiko Tani, Shuji Matsuura and S. ichi Nakashima, "Emission Characteristics Of Photoconductive Antennas Based On Low-Temperature-Grown GaAs And Semi-Insulating GaAs," Optical Society of America **36**, 7853–7859 (1997).

36. Y. Cai, I. Brener, J. Lopata, J. Wynn, L. Pfeiffer, and J. Federici, "Design And Performance Of Singular Electric Field Terahertz Photoconducting Antennas," Applied Physics Letters **71**, 2076–2078 (1997).

37. H. Nyquist, "Thermal Agitation of Electric Charge in Conductors," Phys. Rev. **32**, 110–113 (1928).

38. J. B. Johnson, "Thermal Agitation of Electricity in Conductors," Phys. Rev. **32**, 97–109 (1928).

39. M. Tani, K. Sakai, and H. Mimura, "Ultrafast Photoconductive Detectors Based on Semi-Insulating GaAs and InP," Japanese Journal of Applied Physics **36**, 1175 (1997).

40. E. Moreno, M. Pantoja, F. Ruiz, J. Roldán, and S. García, "On The Numerical Modeling Of Terahertz Photoconductive Antennas," Journal of Infrared, Millimeter, and Terahertz Waves **35**, 432–444 (2014).

41. N. Vieweg, M. Mikulics, M. Scheller, K. Ezdi, R. Wilk, H.-W. Hubers, and M. Koch, "Enhanced emission from THz antennas made of low-temperature-grown GaAs with annealed ohmic contacts," in "Infrared, Millimeter and Terahertz Waves, 2008. IRMMW-THz 2008. 33rd International Conference on," (2008), pp. 1–2.

42. T. Martin, "An Improved Near- To Far-Zone Transformation For The Finite-Difference Time-Domain Method," Antennas and Propagation, IEEE Transactions on **46**, 1263 –1271 (1998).

43. M. C. Hoffmann, "Novel Techniques in THz-Time-Domain-Spectroscopy - A comprehensive study of technical improvements to THz-TDS," Ph.D. thesis, Mathematik und Physik der Albert-Ludwigs-Universit (2006).

44. M. Tani, Y. Hirota, C. Que, S. Tanaka, R. Hattori, M. Yamaguchi, S. Nishizawa, and M. Hangyo, "Novel Terahertz Photoconductive Antennas," International Journal of Infrared and Millimeter Waves **27**, 531–546 (2006).

45. R. . A. Cheville, *Terahertz Spectroscopy Principles And Applications* (CRC Press, 2007).

46. D. Saeedkia, "Terahertz Photoconductive Antennas: Principles And Applications," in "Antennas and Propagation (EUCAP), Proceedings of the 5th European Conference on," (2011), pp. 3326–3328.

47. S. B. Damelin and W. M. Jr, *The Mathematics of Signal Processing* (Cambridge University Press, 2012).

48. B. E. S. M.C.Teich, *Fundamentals Of Photonics* (Wiley Series in Pure and Applied Optics, 2007).

49. M. Han, R. Dutton, and S. Fan, "Model dispersive media in finite-difference time-domain method with complex-conjugate pole-residue pairs," Microwave and Wireless Components Letters, IEEE **16**, 119–121 (2006).

50. S. Selberherr, *Analysis And Semiconductor Devices* (Springer-Verlag, 1984).